

Finite-Size Scaling of the Full Eigenstate Thermalization in Quantum Spin Chains

Yuke Zhang¹ and Pengfei Zhang^{1, 2, *}

¹*State Key Laboratory of Surface Physics & Department of Physics, Fudan University, Shanghai, 200438, China*

²*Hefei National Laboratory, Hefei 230088, China*

(Dated: February 3, 2026)

Despite the unitary evolution of closed quantum systems, long-time expectation of local observables are well described by thermal ensembles, providing the foundation of quantum statistical mechanics. A promising route to understanding this quantum thermalization is the eigenstate thermalization hypothesis (ETH), which posits that individual energy eigenstates already appear locally thermal. Subsequent studies have extended this concept to the full ETH, which captures higher-order correlations among matrix elements through nontrivial relations. In this work, we perform a detailed exact-diagonalization study of finite-size corrections to these relations in the canonical ensemble. We distinguish two distinct sources of corrections: those arising from energy fluctuations, which decay polynomially with system size, and those originating from fluctuations within each energy window, which decay exponentially with system size. In particular, our analysis resolves the puzzle that, for certain observables, finite-size corrections exhibit anomalous growth with increasing system size even in chaotic systems. Our results provide a systematic and practical methodology for validating the full ETH in quantum many-body systems.

I. INTRODUCTION

Understanding how isolated quantum many-body systems approach thermal equilibrium is a central problem in quantum statistical mechanics. Unlike classical systems, whose thermalization follows from ergodic motion in phase space, the unitary dynamics of closed quantum systems preserves information, challenging the emergence of statistical ensembles. A widely accepted resolution is provided by the eigenstate thermalization hypothesis (ETH), which posits that individual many-body eigenstates already encode thermal behavior for local observables [1–7]. Specifically, for a few-body operator O in the energy eigenbasis $\{|E_i\rangle\}$, ETH asserts

$$O_{ij} = O(E_i) \delta_{ij} + e^{-S(E^+)/2} F_{E^+}^{(2)}(\omega_{ij}) R_{ij}, \quad (1)$$

where $E^+ = (E_i + E_j)/2$, $\omega_{ij} = E_i - E_j$, $O(E)$ gives the thermal expectation value, $S(E)$ is the thermodynamic entropy, $F_E^{(2)}(\omega)$ is a smooth function decaying at large ω , and R_{ij} is a Gaussian random variable with zero mean and unit variance. The diagonal term ensures that long-time averages reproduce thermal predictions, while the exponentially small off-diagonal fluctuations drive equilibration under generic dynamics [4, 7–14]. Experimental demonstrations of quantum thermalization have also been performed in optical lattices [15, 16]. Subsequently, understanding mechanisms that prevent quantum thermalization has become an important topic, highlighting phenomena such as integrability [8, 12, 17–25], many-body localization [26–39], and nonunitary dynamics generated by repeated measurements [40–48].

Nevertheless, the traditional ETH ansatz fails to capture nontrivial higher-order correlation functions, since

all cumulants vanish for Gaussian random variables. To overcome this limitation, the full ETH was introduced [49], in which R_{ij} is treated as a more general random variable. Rather than specifying the underlying distribution of R_{ij} , the full ETH is formulated directly in terms of averaged products of matrix elements:

$$\overline{O_{i_1 i_2} O_{i_2 i_3} \cdots O_{i_q i_1}} = e^{-(q-1)S(E^+)} F_{E^+}^{(q)}(\boldsymbol{\omega}). \quad (2)$$

Here, we assume $i_1 \neq i_2 \cdots \neq i_q$, introduce the relative energies $\boldsymbol{\omega} = (\omega_{i_1 i_2}, \omega_{i_2 i_3}, \dots, \omega_{i_{q-1} i_q})$ with $\omega_{i_m i_n} = E_{i_m} - E_{i_n}$, and extend the definition of the center-of-mass energy to $E^+ = \sum_{m=1}^q E_{i_m}/q$. The statistical average may be understood as an average over individual energy levels within a narrow energy window. In addition, the full ETH assumes

$$\overline{O_{i_1 i_2} \cdots O_{i_{k-1} i_1} O_{i_1 i_{k+1}} \cdots O_{i_q i_1}} = \overline{O_{i_1 i_2} \cdots O_{i_{k-1} i_1}} \overline{O_{i_1 i_{k+1}} \cdots O_{i_q i_1}}. \quad (3)$$

Later developments further highlight the connection between full ETH and free probability [50–57], which identifies free cumulants as the fundamental ingredients governing higher-order correlation functions. Analytical and numerical studies of full ETH and its violations have been carried out in Refs. [51, 57–60]. In particular, the factorization correction for non-integrable Floquet systems is discussed in [57]. However, a careful finite-size scaling analysis of the corrections to these relations in energy conserved systems remains lacking.

In this work, we perform a systematic finite-size scaling analysis of the full ETH in concrete quantum spin chains, considering both single-site and two-site observables. Following Ref. [51], we focus on finite-size corrections to correlation functions in the canonical ensemble, as elaborated below, rather than working directly with the matrix-element relations in Eqs. (2) and (3). We decompose the finite-size corrections of correlation functions into distinct contributions, including those arising from energy fluctuations, which decay polynomially

* PengfeiZhang.physics@gmail.com

with system size, and those originating from fluctuations within each energy window, which decay exponentially with system size. In particular, the contribution from fluctuations within each energy window can be predicted using thermal density matrices. This decomposition also clearly demonstrates the validity of the full ETH in chaotic spin chains, despite the fact that corrections to certain correlation functions—those involving multiple summations with different scalings—can exhibit anomalous growth with increasing system size at moderate system sizes. Our results provide a refined understanding of the full ETH and a practical methodology for validating it using exact diagonalization.

II. FULL EIGENSTATE THERMALIZATION FOR CORRELATION FUNCTIONS

We now describe our setup by revisiting the predictions of the full ETH for correlation functions [49, 50]. We primarily focus on multitime correlation functions of an operator O at infinite temperature, which are defined as

$$C^{(q)}(t_1, t_2, \dots, t_{q-1}) \equiv \langle O(t_1) \cdots O(t_{q-1}) O(0) \rangle. \quad (4)$$

Here, the expectation value is taken over the infinite-temperature ensemble with density matrix $\rho = \mathbb{1}/D$, where D is the Hilbert space dimension. The operator is evolved under Heisenberg evolution $O(t) = e^{iHt} O e^{-iHt}$ with Hamiltonian H .

A. Two-point function

To see how the correlation function is related to the full ETH ansatz (2) and (3), we first consider the case $q = 2$, which reads $C^{(2)}(t) = D^{-1} \sum_{ij} e^{i\omega_{ij} t} O_{ij} O_{ji}$ [61]. To employ the full ETH ansatz (2) and (3), we separate the summation into contributions with $j = i$ and those with $j \neq i$, which gives

$$C^{(2)}(t) = k_2(t) - \frac{1}{D} \sum_i O_{ii}^2. \quad (5)$$

Here, we introduce the free cumulants k_q , which are fundamental objects in free probability theory [50]:

$$k_q(t) = \frac{1}{D} \sum_{i_1 \neq i_2 \neq \dots \neq i_q} e^{i\omega \cdot t} O_{i_1 i_2} O_{i_2 i_3} \cdots O_{i_q i_1}, \quad (6)$$

with $t = (t_1, t_2, \dots, t_{q-1})$. In the second term of (5), the summation over individual eigenstates within each narrow energy window effectively plays the role of the averaging in (2) and (3), which identifies $\frac{1}{D} \sum_i O_{ii}^2 = \frac{1}{D} \sum_i \overline{O_{ii}^2}$. To proceed, there are two key steps:

1. We apply the factorization in (3), which yields the approximation $\overline{O_{ii}^2} \approx \overline{O_{ii}}^2$.

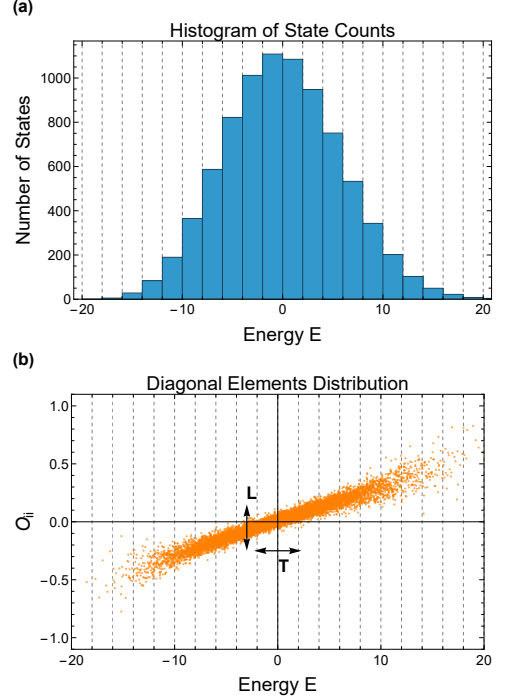


FIG. 1. An illustration of the decomposition of finite-size corrections introduced in this work. In panel (a), we introduce a series of narrow energy windows with a fixed width $\Delta = 2$ that is independent of the system size. In panel (b), we illustrate the distribution of O_{ii} over all eigenstates, where the total variance consists of the variance within each energy window (longitudinal direction, denoted as L) and the variance between different energy windows (transverse direction, denoted as T).

2. We note that the summation over i effectively fixes the energy E_i near that of the infinite-temperature ensemble under the saddle-point approximation. The same energy fixing can be implemented by

$$\frac{1}{D} \sum_i \overline{O_{ii}}^2 \approx \left(\frac{1}{D} \sum_i \overline{O_{ii}} \right)^2 = k_1^2. \quad (7)$$

Putting all ingredients together, we find the ETH prediction $C^{(2)}(t) \approx k_2(t) - k_1^2 \equiv C_{\text{ETH}}^{(2)}(t)$.

The above analysis provides a natural decomposition of the finite-size corrections. We introduce the error of the two-point function as

$$F_{11} \equiv C_{\text{ETH}}^{(2)}(t) - C^{(2)}(t) = \frac{1}{D} \sum_i O_{ii}^2 - \left(\frac{1}{D} \sum_i O_{ii} \right)^2, \quad (8)$$

which measures the variance of all diagonal elements O_{ii} across the full spectrum of eigenstates. In step 1, we neglect fluctuations of O_{ii} across individual energy levels within each small energy window, which are expected to be exponentially small in the system size L [7, 62]. In step 2, we neglect subleading corrections arising from the saddle-point approximation, which originate from energy

fluctuations with $\delta E/E \sim O(1/\sqrt{L})$ [63, 64]. Therefore, we expect the corresponding contribution to scale polynomially with system size, as explicitly analyzed below. Motivated by these considerations, we introduce a decomposition into longitudinal and transverse variances, $F_{11} = F_{11}^L + F_{11}^T$, where

$$\begin{aligned} F_{11}^L &\equiv \sum_E P_E \left[\frac{1}{d_E} \sum_{i \in E} O_{ii}^2 - \left(\frac{1}{d_E} \sum_{i \in E} O_{ii} \right)^2 \right], \\ F_{11}^T &\equiv \sum_E P_E \left[\left(\frac{1}{d_E} \sum_{i \in E} O_{ii} \right)^2 \right] - \left[\sum_E P_E \left(\frac{1}{d_E} \sum_{i \in E} O_{ii} \right) \right]^2. \end{aligned} \quad (9)$$

Here, we introduce a series of narrow energy windows for the eigenenergies of the Hamiltonian H with width Δ , as sketched in FIG. 1. We denote the number of eigenstates in the window centered around E by d_E , and define $P_E = d_E/D$ as a normalized probability distribution. By definition, F_{11}^L measures the variance of O_{ii} within each energy window, weighted by the corresponding probability. In contrast, F_{11}^T measures the variance between different energy windows.

While the analysis of F_{11}^L requires numerical simulations, the scaling of F_{11}^T in the thermodynamic limit can be computed using thermal ensembles. This is because the average within each energy window is equivalent to a microcanonical ensemble average, and the number of states scales as $d_E \sim e^{S(E)}$. Therefore, we have

$$F_{11}^T = \frac{1}{D} \int dE e^{S(E)} [O(E) - O(0)]^2. \quad (10)$$

Here, $O(E)$ denotes the expectation value of the operator O in the microcanonical ensemble at energy E . We assume that the infinite-temperature ensemble corresponds to energy $E = 0$, which can always be achieved by shifting the Hamiltonian H by a constant. Since $S(E)$ has a maximum near $E = 0$, performing a Taylor expansion yields

$$F_{11}^T \approx \int dE e^{-\frac{E^2}{2C_0}} [\partial_E O(0)]^2 E^2 \approx C_0 [\partial_E O(0)]^2. \quad (11)$$

Here, $C_0 = C_V/\beta^2 \propto L$ is extensive, where C_V is the specific heat in the infinite-temperature limit. We have used the fact that $e^{S(0)} = D$. The derivative $\partial_E O(0)$ scales as $1/L$, since $O(E) \sim O(1)$ for local observables and the energy is extensive. As a consequence, we conclude that $F_{11}^T \propto L^{-1}$ when $\partial_E O(0) \neq 0$. For systems with $\partial_E O(0) = 0$, higher-order expansions must be considered, which lead to a smaller F_{11}^T . Nevertheless, we expect that the result still scales polynomially with the system size L .

B. Higher-order correlation function

Next, we generalize the above discussion to higher-order correlation functions. In this work, we focus on

the cases $q = 3$ and $q = 4$. For $q = 3$, the full ETH predicts the relation [49, 50]

$$\begin{aligned} C^{(3)}(t_1, t_2) &\approx k_3(t_1, t_2) + [k_2(t_1 - t_2) \\ &+ k_2(t_1) + k_2(t_2)] k_1 + k_1^3 \equiv C_{\text{ETH}}^{(3)}(t_1, t_2). \end{aligned} \quad (12)$$

The approximation arises from two contributions: (1) replacing the summation $D^{-1} \sum_i O_{ii}^3$ with $k_1^3 = (D^{-1} \sum_i O_{ii})^3$, and (2) replacing the summation $D^{-1} \sum_{i \neq j} e^{i\omega_{ij}t} |O_{ij}|^2 O_{ii}$ with

$$k_2(t) k_1 = \frac{1}{D} \sum_{i \neq j} e^{i\omega_{ij}t} |O_{ij}|^2 \times \frac{1}{D} \sum_k O_{kk}.$$

Since correlation functions generally decay with time t , we introduce error terms evaluated at $t = 0$ to benchmark the finite-size corrections as

$$\begin{aligned} F_{111} &= \frac{1}{D} \sum_i O_{ii}^3 - \left(\frac{1}{D} \sum_i O_{ii} \right)^3, \\ F_{21} &= \frac{1}{D} \sum_{i \neq j} |O_{ij}|^2 O_{ii} - k_2(0) k_1. \end{aligned} \quad (13)$$

For F_{111} , it measures how the third-order moment deviates from the expectation value. We can perform a decomposition into longitudinal and transverse components similar to (9), writing $F_{111} = F_{111}^L + F_{111}^T$, where

$$\begin{aligned} F_{111}^L &\equiv \sum_E P_E \left[\frac{1}{d_E} \sum_{i \in E} O_{ii}^3 - \left(\frac{1}{d_E} \sum_{i \in E} O_{ii} \right)^3 \right], \\ F_{111}^T &\equiv \sum_E P_E \left[\left(\frac{1}{d_E} \sum_{i \in E} O_{ii} \right)^3 \right] - \left[\sum_E P_E \left(\frac{1}{d_E} \sum_{i \in E} O_{ii} \right) \right]^3. \end{aligned} \quad (14)$$

Similar to the analysis in previous subsection, F_{111}^T can also be expressed using thermodynamical quantities, and a direct scaling analysis gives $F_{111}^T \lesssim O(L^{-2})$ by expanding $S(E)$ to the order of E^3 . For F_{21} , it is not an independent quantity for operators satisfying $O^2 = \mathbb{1}$, which we focus on from now on. Indeed, we have $F_{21} = -m_3 + m_1 m_2$, where $m_k = D^{-1} \sum_i O_{ii}^k$. In particular, for Pauli operators with $m_1 = 0$, this reduces to $F_{21} = -m_3 = -F_{111}$.

Finally, the finite-size corrections for $C^{(4)}(t_1, t_2, t_3)$ can be introduced analogously. Again, we focus only on the error terms at $t_1 = t_2 = t_3 = 0$, which include six additional quantities. Firstly, we have an error term

$$F_{1111} = \frac{1}{D} \sum_i O_{ii}^4 - \left(\frac{1}{D} \sum_i O_{ii} \right)^4 = m_4 - m_1^4, \quad (15)$$

We take F_{1111} as an independent contribution to be analyzed, whose transverse component, defined analogously to (9) and (14), is expected to scale as L^{-2} :

$$F_{1111}^T \approx \int dE e^{-\frac{E^2}{2C_0}} [\partial_E O(0)]^4 E^4 \approx 3C_0^2 [\partial_E O(0)]^4. \quad (16)$$

Secondly, we have a new type of error, known as crossing diagram [49–51], defined as $C = D^{-1} \sum_{i \neq j} |O_{ij}|^4$. It is argued that C decays exponentially with system size L [49–51]. In addition, we have other four error terms:

$$F_{22} = \frac{1}{D} \sum_{i \neq j \neq k} O_{ij} O_{ji} O_{ik} O_{ki} - k_2(0)^2 = m_4 - m_2^2 - C, \quad (17)$$

$$F_{31} = \frac{1}{D} \sum_{i \neq j \neq k} O_{ij} O_{jk} O_{ki} O_{ii} - k_3(0, 0) k_1 = -m_2 + 2m_4 + m_1(m_1 + m_2 - 2m_3) - P, \quad (18)$$

$$F_{211}^{(1)} = \frac{1}{D} \sum_{i \neq j} O_{ii}^2 O_{ij} O_{ji} - k_2(0) k_1^2 = m_2 - m_4 - m_1^2(1 - m_2), \quad (19)$$

$$F_{211}^{(2)} = \frac{1}{D} \sum_{i \neq j} O_{ii} O_{jj} O_{ij} O_{ji} - k_2(0) k_1^2 = -m_4 - m_1^2(1 - m_2) + P. \quad (20)$$

These terms quantify the factorization relation in (3), which includes loops of indices with $k > 1$. For conciseness, we introduce $P = \frac{1}{D} \sum_{ij} O_{ij} O_{ji} O_{ii} O_{jj}$, which is the only new ingredient in addition to F_{1111} and C . Theoretically, all error terms should vanish in the thermodynamical limit using the saddle-point analysis [50]. As a result, we expect these terms to decay polynomially with system size. However, the complex structures in these equations make their finite-size scaling extremely difficult to identify without the decomposition into m_k , C , and P , as explicitly demonstrated in the next section. As a result, we will present numerical results for all of these error terms.

III. NUMERICAL RESULTS

In this section, we present numerical results for the error terms and their decompositions defined in the previous section. We consider the mixed field Ising model:

$$\hat{H} = J \sum_{i=1}^L Z_i Z_{i+1} + w \sum_{i=1}^L X_i + h \sum_{i=1}^L Z_i. \quad (21)$$

We choose $J = 1$, $w = 1.05$, and $h = \frac{\sqrt{5}-1}{2}$ to place the model in the chaotic regime [65–73]. Focusing on open boundary conditions, the system exhibits reflection symmetry. We therefore restrict our analysis to the $+1$ parity sector and consider only operators that are invariant under the parity transformation. In the Appendix A, we present a parallel discussion of the random-field XXZ model, which does not exhibit the reflection symmetry. The results for both models are qualitatively the same.

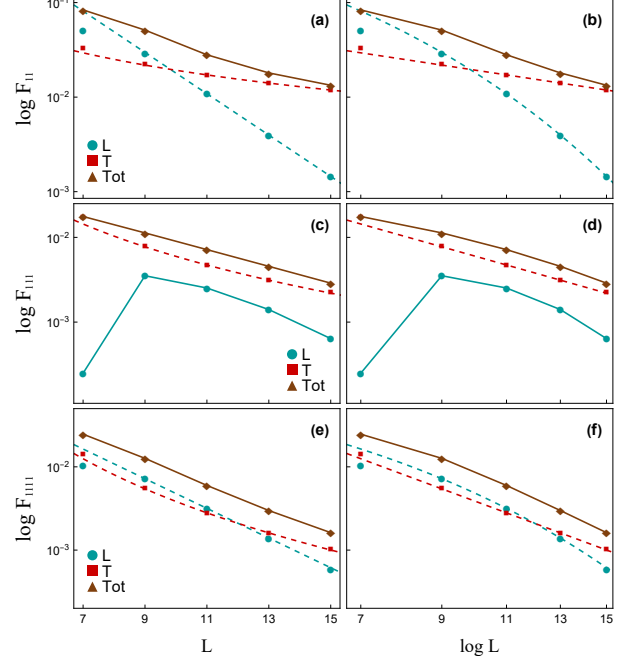


FIG. 2. Numerical results for the error terms F_{11} , F_{111} , and F_{1111} of the mixed-field Ising model as a function of system size L (odd) for the single-site operator $O = Z_{(L+1)/2}$. Here, we fix the width of the energy window to $\Delta = 2$. The results are presented in both log plots and log–log plots. The dashed lines correspond to fits to the last four data points, as described in the main text, while the solid lines serve as guides to the eye.

A. Single-site operator

We now present results for a single-site operator. We focus on systems with odd L and choose the operator to be the Pauli- Z operator at the center, $O = Z_{(L+1)/2}$. The corresponding first moment, m_1 , remains zero even after fixing the parity sector. Following the previous discussion, we first investigate the error terms $F_{11} = m_2$, $F_{111} = m_3$, and $F_{1111} = m_4$, which correspond to moments of the diagonal matrix elements. The results are presented in FIG. 2 using both log plots and log–log plots. From the raw data for both F_{11} and F_{1111} , we already observe that the longitudinal components decay exponentially with system size, corresponding to straight lines in the log plots. Therefore, we perform fits of the form $a \exp(-bL)$ to these curves using the last four data points, and the results are shown as green dashed lines. For F_{111} , the results exhibit a faster-than-exponential decay, as indicated by the increasing slope in the log plot. This behavior originates from cancellations between terms with positive and negative O_{ii} .

On the other hand, the raw data in the transverse direction all exhibit power-law decay, as demonstrated by the log–log plots. We therefore fit the data with a/L^b , and the results are shown as red dashed lines. For F_{11} ,

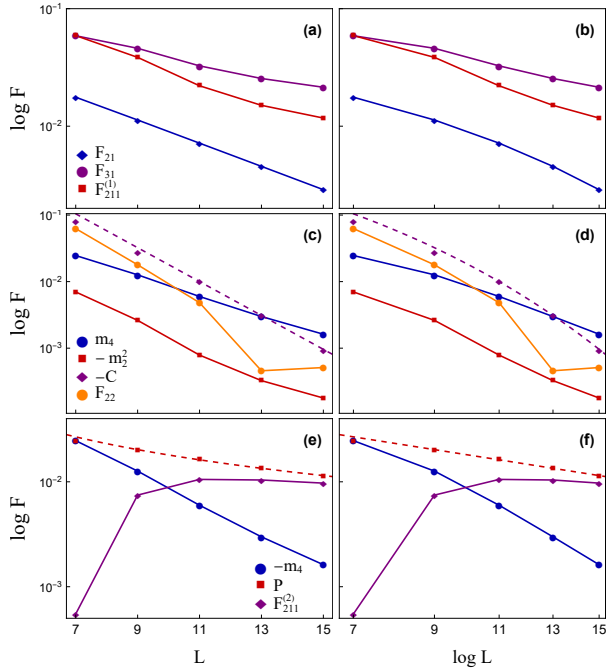


FIG. 3. Numerical results for the error terms F_{21} , F_{31} , $F_{211}^{(1)}$, F_{22} , and $F_{211}^{(2)}$ of the mixed-field Ising model as a function of system size L (odd) for the single-site operator $O = Z_{(L+1)/2}$ with $\Delta = 2$. The results are presented in both log plots and log-log plots. The dashed lines correspond to fits to the last four data points, as described in the main text, while the solid lines serve as guides to the eye.

F_{111} , and F_{1111} , the resulting exponents b are 1.1890, 2.4640, and 3.3120, respectively (see TABLE. I), which include finite-size corrections to the theoretical predictions of 1, 2, and 2 presented in the previous section. Nevertheless, the power-law behavior is already evident despite the moderate system sizes. We further emphasize that the decomposition into longitudinal and transverse components is crucial for clearly validating the finite-size scaling of F_{11} , F_{111} and F_{1111} . Without this decomposition, the total error term does not exhibit a clear scaling form, since contributions from different components are comparable at the accessible system sizes.

Next, we proceed to other error terms, including F_{21} , F_{31} , $F_{211}^{(1)}$, F_{22} , and $F_{211}^{(2)}$. The results are presented in FIG. 3. First, the results for F_{21} , F_{31} , and $F_{211}^{(1)}$ decay monotonically with system size. In particular, both F_{21} and $F_{211}^{(1)}$ depend only on the moments m_k , which have already been analyzed in FIG. 2. As a result, we conclude that they all decay polynomially with the system size L in the large- L limit, although this behavior is not evident in finite-size data without the decomposition. The result for F_{31} contains a new ingredient, P , which is shown in panels (e-f). We find that P also exhibits power-law decay with system size L , and the corresponding fitting results (shown in dashed lines in FIG. 3 (e-f)) are presented in

TABLE I. Fitted parameters for the single-site operator $O = Z_{(L+1)/2}$ of the mixed-field Ising model.

Component	Model Expression	a	b
F_{11}^L	$a \exp(-bL)$	2.7530	0.5032
F_{11}^T	a/L^b	0.2975	1.1890
F_{111}^L	$a \exp(-bL)$	—	—
F_{111}^T	a/L^b	1.7390	2.4640
F_{1111}^L	$a \exp(-bL)$	0.2895	0.4104
F_{1111}^T	a/L^b	7.8840	3.3120
C	$a \exp(-bL)$	6.3150	0.5861
P	a/L^b	0.2346	1.1150

Table I. This indicates that the dominant contribution to P also originates from energy fluctuations.

Finally, numerical results for F_{22} and $F_{211}^{(2)}$ are presented in FIG. 3(cf). Surprisingly, these results exhibit anomalous growth as the system size increases to $L = 15$, which naively indicates a violation of the full ETH, despite the fact that the quantum spin chain is chaotic. As we mentioned in the previous discussions, the important observation to resolve this puzzle is the existence of multiple terms. For $m_1 = 0$, the relations in (17) becomes

$$F_{22} = m_4 - m_2^2 - C, \quad F_{211}^{(2)} = -m_4 + P. \quad (22)$$

If we plot the results for each component individually, they show clear decay as the system size increases. As elaborated in FIG. 2, both m_4 and m_2 exhibit combinations of exponential and power-law decay with system size L . The results for C also clearly show exponential decay with L , as indicated by the fits shown using the purple dashed lines. However, when these components are combined to obtain F_{22} , the result exhibits a kink due to an interchange of the dominant contributions at accessible system sizes. A similar phenomenon occurs for $F_{211}^{(2)}$. Our results highlight the importance to analyze individual contributions for validating the full ETH in quantum lattice systems.

B. Two-site operator

We next consider a two-site operator for systems with even L . We choose the operator to be $O = Z_{L/2}Z_{L/2+1}$. While the first moment m_1 vanishes in the full Hilbert space, it becomes nonzero when restricted to states with even parity. To obtain $m_1(L)$, we first focus on the pair of qubits at sites $L/2$ and $L/2+1$. There are two states, $|\uparrow\uparrow\rangle$ and $|\downarrow\downarrow\rangle$, with eigenvalue $Z_{L/2}Z_{L/2+1} = 1$; both states have even parity. There are also two states, $\frac{1}{\sqrt{2}}(|\uparrow\downarrow\rangle + |\downarrow\uparrow\rangle)$ and $\frac{1}{\sqrt{2}}(|\uparrow\downarrow\rangle - |\downarrow\uparrow\rangle)$, with eigenvalue -1 , and only one of them has even parity. Therefore, we expect

$$m_1(L) = \frac{D_{\text{even}}(L-2) - D_{\text{odd}}(L-2)}{3D_{\text{even}}(L-2) + D_{\text{odd}}(L-2)}. \quad (23)$$

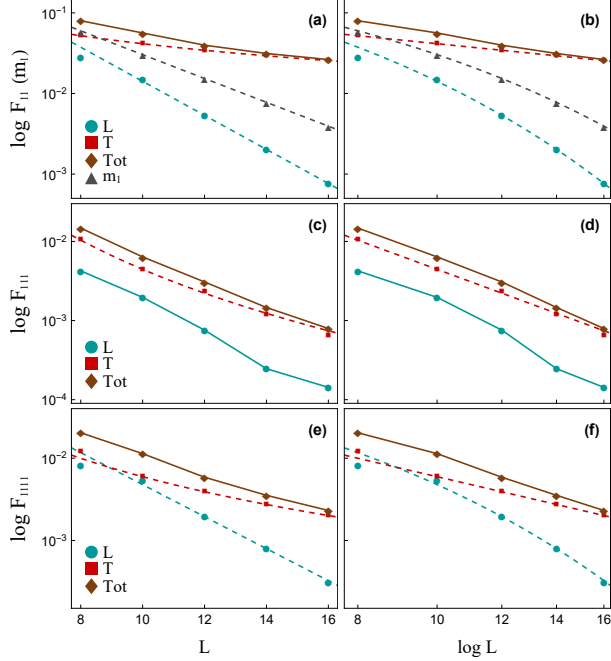


FIG. 4. Numerical results for the error terms F_{11} , F_{111} , and F_{1111} of the mixed-field Ising model as a function of the system size L (even) for the two-site operator $O = Z_{L/2}Z_{L/2+1}$. We fix the width of the energy window to $\Delta = 2$. The results are presented in both log plots and log-log plots. The dashed lines correspond to fits to the last four data points, while the solid lines serve as guides to the eye.

Here, $D_{\text{even}}(L-2)$ and $D_{\text{odd}}(L-2)$ denote the dimensions of the Hilbert spaces with even and odd parity, respectively, for the remaining $L-2$ qubits. To proceed, we perform a similar analysis by adding a pair of qubits to derive the recursion relations for $D_{\text{even}}(L-2)$ and $D_{\text{odd}}(L-2)$, which read

$$\begin{aligned} D_{\text{even}}(L) &= 3D_{\text{even}}(L-2) + D_{\text{odd}}(L-2), \\ D_{\text{odd}}(L) &= 3D_{\text{odd}}(L-2) + D_{\text{even}}(L-2). \end{aligned} \quad (24)$$

The solution gives $D_{\text{even/odd}}(L) = 2^{L-1} \pm 2^{\frac{L}{2}-1}$. As a result, we find $m_1(L) = \frac{1}{2^{L/2+1}}$, which decays exponentially with system size L .

With this knowledge, we proceed to the numerical results for $F_{11} = m_2 - m_1^2$, $F_{111} = m_3 - m_1^3$, and $F_{1111} = m_4 - m_1^4$. The results, shown in Fig. 4, are analogous to those obtained for the single-site operator in the previous section: the longitudinal component decays exponentially with L , while the transverse component decays polynomially. The only exception is F_{111}^L . Unlike the single-site case, the slope in the log plot exhibits non-monotonic behavior. Nevertheless, since $|m_3| < m_2$ due to $|O_{ii}| < 1$, the decay of F_{111}^L is controlled by that of F_{11}^L and at most polynomial in the system size L . The results for the error terms F_{21} , F_{31} , $F_{211}^{(1)}$, F_{22} , and $F_{211}^{(2)}$ are presented in Fig. 5. The error terms F_{21} , F_{31} , and

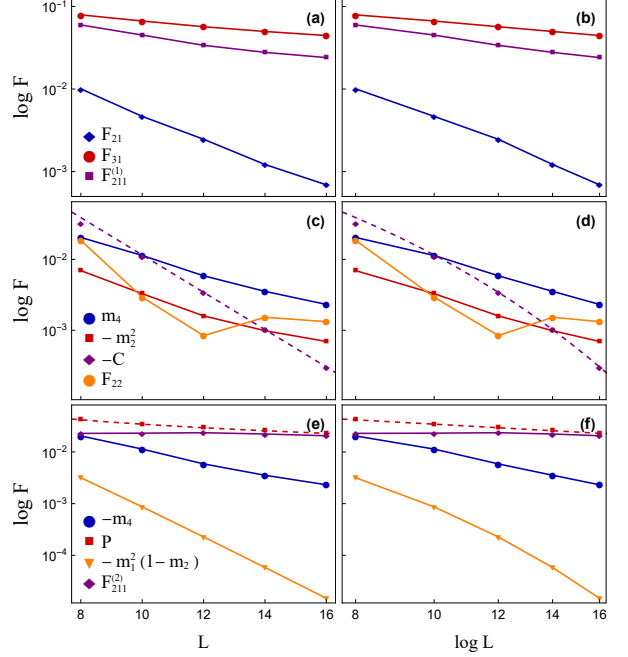


FIG. 5. Numerical results for the error terms F_{21} , F_{31} , $F_{211}^{(1)}$, F_{22} , and $F_{211}^{(2)}$ of the mixed-field Ising model as a function of the system size L (even) for the two-site operator $O = Z_{L/2}Z_{L/2+1}$, with $\Delta = 2$. The results are presented in both log plots and log-log plots. The dashed lines correspond to fits to the last four data points, while the solid lines serve as guides to the eye.

$F_{211}^{(1)}$ decay monotonically as functions of the system size L . In contrast, F_{22} and $F_{211}^{(2)}$ again exhibit anomalous growth in the accessible system sizes. Nevertheless, each individual component shows a clear monotonic decrease as L increases. In particular, the fitted parameters for each components are presented in TABLE. II. This behavior clearly demonstrates the validity of the full ETH for the two-site operator.

TABLE II. Fitted parameters for the two-site operator $O = Z_{L/2}Z_{L/2+1}$ of the mixed-field Ising model.

Component	Model	Expression	a	b
m_1		$a \exp(-bL)$	0.9132	0.3405
F_{11}^L		$a \exp(-bL)$	1.8370	0.4865
F_{11}^T		a/L^b	0.4393	1.0250
F_{111}^L		$a \exp(-bL)$	—	—
F_{111}^T		a/L^b	28.1200	3.8020
F_{1111}^L		$a \exp(-bL)$	0.4197	0.4477
F_{1111}^T		a/L^b	1.2180	2.3100
C		$a \exp(-bL)$	4.9650	0.6063
P		a/L^b	0.2535	0.8670

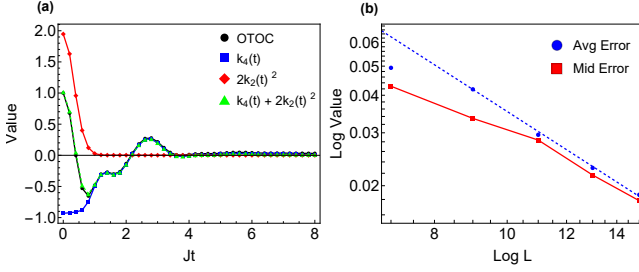


FIG. 6. Numerical results for the finite-size corrections of the OTOC for the single-site operator $O = Z_{(L+1)/2}$. In panel (a), we present the numerical results at $L = 15$ for the OTOC, the free cumulants, and the prediction from the full ETH. In panel (b), we show the finite-size corrections for both the averaged and mid-time errors.

C. Finite-size corrections at finite times

In the previous discussion, we only considered finite-size corrections at $t = 0$. In this subsection, we examine the finite-size scaling of the error at nonzero times. We focus on the single-site operator $O = Z_{(L+1)/2}$ for $q = 4$ with $k_1 = m_1 = 0$. We consider the out-of-time-order correlator (OTOC), defined as [74–80]

$$\text{OTOC}(t) \equiv C^{(4)}(t, 0, t) = \langle O(t)O(0)O(t)O(0) \rangle. \quad (25)$$

Using the full ETH, the OTOC can be related to free cumulants as (for $k_1 = 0$):

$$\text{OTOC}(t) \approx k_4(t, 0, t) + 2k_2(t)^2 \equiv \text{OTOC}_{\text{ETH}}(t). \quad (26)$$

We numerically benchmark the deviation between $\text{OTOC}_{\text{ETH}}(t)$ and $\text{OTOC}(t)$ using two criteria, which capture either the averaged error or the error at a single time. The averaged error is defined as

$$E_{\text{avg}} = \left| \frac{1}{T} \int_0^T dt [\text{OTOC}_{\text{ETH}}(t) - \text{OTOC}(T/2)] \right|. \quad (27)$$

Here, we choose a cutoff time T . For the single-time error, we focus on the time $T/2$, which we refer to as the mid-time error, defined as $E_{\text{Mid}} = |\text{OTOC}_{\text{ETH}}(T/2) - \text{OTOC}(T/2)|$. The numerical results are presented in FIG. 6 for $T = 8$, which suggests that both errors decay polynomially in system size. Using the last four data points, we fit the averaged error with a/L^b , obtaining $a \approx 1.4$ and $b \approx 1.6$, as shown by the blue dashed lines. These results further support the validity of the full ETH at finite evolution times t .

IV. DISCUSSIONS

In summary, we have performed a comprehensive numerical study of finite-size corrections to the full eigenstate thermalization hypothesis in chaotic quantum spin

chains. By decomposing error terms into longitudinal components, which capture fluctuations within narrow energy windows, and transverse components, which capture fluctuations across different energy windows, we identified their distinct scaling behaviors. Our results show that longitudinal contributions decay exponentially with system size, while transverse contributions follow power-law scaling consistent with thermodynamic predictions. Importantly, we resolved apparent anomalies in certain higher-order correlation functions, demonstrating that these are finite-size effects arising from the interplay of multiple contributions rather than genuine violations of the full ETH. The decomposition framework and systematic finite-size analysis presented here provide a practical and reliable methodology for validating the full ETH in both single-site and multi-site observables, offering insights into the emergence of thermal behavior in finite quantum systems.

We conclude our work with several remarks. First, a detailed analysis at finite temperatures may reveal additional structures in the finite-size scaling behavior, potentially offering new insights into the thermalization process in quantum many-body systems. Second, it is natural to ask whether energy conservation significantly affects the finite-size scaling; this question could be addressed by studying eigenstates of chaotic quantum circuit models with and without conservation laws. Third, exploring the finite-size scaling of the full ETH in integrable [58] or localized systems may provide a clearer distinction between these systems and chaotic ones, and help identify universal versus nonuniversal features of quantum thermalization. Finally, understanding how the full ETH manifests in conformal field theories with large central charge [81] could reveal a rich interplay among quantum chaos, holographic duality, and the structure of operator correlations. We leave all these studies to future work.

Acknowledgement. We thank Yanting Cheng and Ning Sun for helpful discussions. This project is supported by the NSFC under grant 12374477, the Shanghai Rising-Star Program under grant number 24QA2700300, and the Quantum Science and Technology-National Science and Technology Major Project 2024ZD0300101.

Appendix A: The random-field XXZ model

In this appendix, we present numerical results for the random-field XXZ model. The Hamiltonian reads

$$\hat{H} = J \sum_{i=1}^L (X_i X_{i+1} + Y_i Y_{i+1}) + J_z \sum_{i=1}^L Z_i Z_{i+1} + \sum_{i=1}^L h_i Z_i. \quad (\text{A1})$$

We focus on open boundary conditions and choose $J = 1$ and $J_z = 1.05$. The random fields h_i are independently sampled from the uniform distribution $[-0.75, 0.75]$, a regime in which the system resides in the thermalized

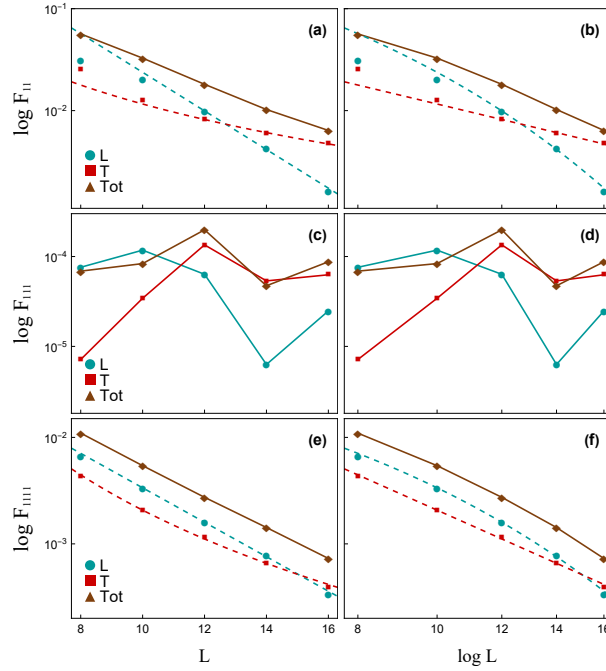


FIG. 7. Numerical results for the error terms F_{11} , F_{111} , and F_{1111} of the random-field XXZ model as a function of system size L for the single-site operator $O = Z_{L/2}$. Here, we fix the width of the energy window to $\Delta = 1$. The results are presented in both log plots and log-log plots. The dashed lines correspond to fits to the last four data points, while the solid lines serve as guides to the eye.

phase [26, 82–86]. Due to the spin rotation symmetry (along the z direction) of the Hamiltonian, we restrict our discussion to the $S_z = 0$ sector. We focus on the same single-site and two-site operators as those employed in the mixed-field Ising model, which are invariant under the spin rotation.

1. Single-site operator

Here, we focus on systems with even L and choose the operator $O = Z_{L/2}$. Similar to the mixed-field Ising model, m_1 remains zero after fixing the spin sector. The numerical results for the error terms $F_{11} = m_2$, $F_{111} = m_3$, and $F_{1111} = m_4$ are presented in FIG. 7. Following the same notation as that for the mixed-field Ising model. The longitudinal and transverse components of F_{11} and F_{1111} decay exponentially and polynomially with L , respectively, which is consistent with the previous conclusion. Accordingly, we perform fits of the form $a \exp(-bL)$ for F_{11}^L , F_{1111}^L , and fits of the form a/L^b for F_{11}^T , F_{1111}^T , in both cases using the last four data points. We find that the behaviors of both longitudinal and transverse components F_{1111}^L , F_{1111}^T are non-monotonic. Nevertheless, as pointed out in the main text, their behaviors should be controlled by that of F_{11}^L

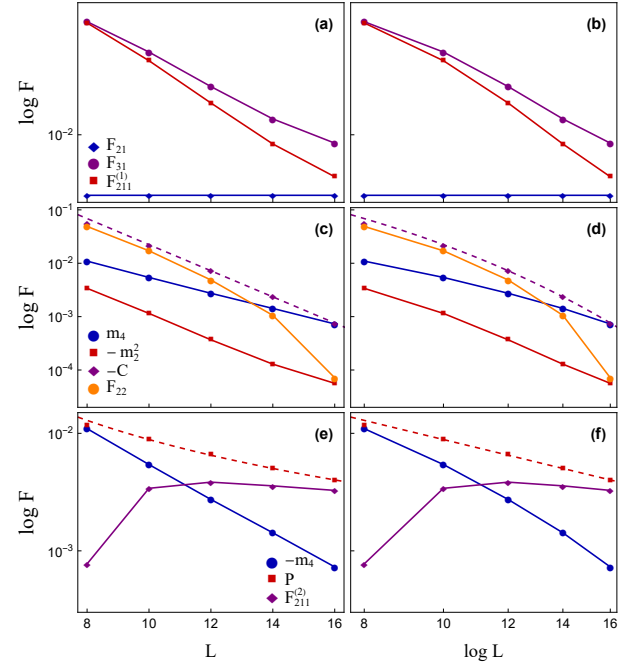


FIG. 8. Numerical results for the error terms F_{21} , F_{31} , $F_{211}^{(1)}$, F_{22} , and $F_{211}^{(2)}$ of the random-field XXZ model as a function of system size L for the single-site operator $O = Z_{L/2}$ with $\Delta = 1$. The results are presented in both log plots and log-log plots. The dashed lines correspond to fits to the last four data points, while the solid lines serve as guides to the eye.

and F_{11}^T , remaining at most polynomial in the system size L . The results for the error terms F_{21} , F_{31} , $F_{211}^{(1)}$, F_{22} , and $F_{211}^{(2)}$ are presented in Fig. 8. Since these terms exhibit behaviors similar to those observed in the mixed-field Ising model, we employ the same decomposition method to analyze F_{22} and $F_{211}^{(2)}$. The fitted parameters for each component are presented in TABLE. III. These results validate the full ETH for the single-site operator.

TABLE III. Fitted parameters for the single-site operator $O = Z_{L/2}$ of the random-field XXZ model.

Component	Model	Expression	a	b
F_{11}^L		$a \exp(-bL)$	1.8600	0.4360
F_{11}^T		a/L^b	0.9643	1.9190
F_{1111}^L		$a \exp(-bL)$	—	—
F_{1111}^T		a/L^b	—	—
F_{11111}^L		$a \exp(-bL)$	0.1394	0.3725
F_{11111}^T		a/L^b	5.4190	3.4170
C		$a \exp(-bL)$	6.2120	0.5630
P		a/L^b	0.4270	1.6830

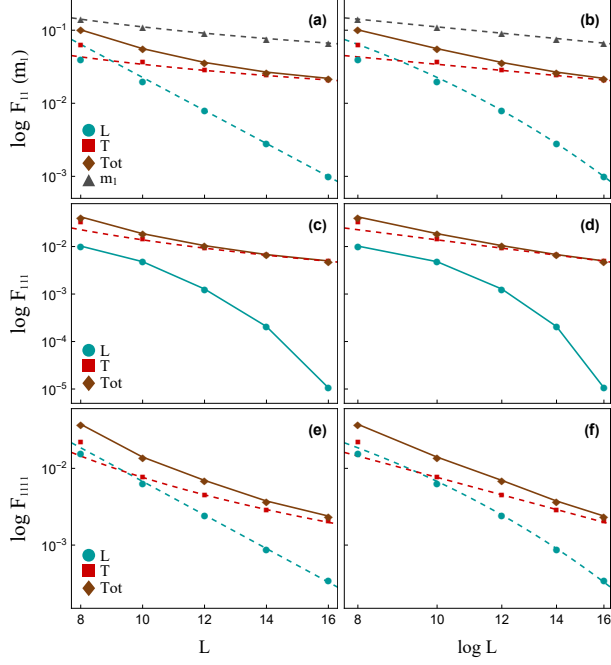


FIG. 9. Numerical results for the error terms F_{11} , F_{111} , and F_{1111} of the random-field XXZ model as a function of system size L for the two-site operator $O = Z_{L/2}Z_{L/2+1}$. Here, we fix the width of the energy window to $\Delta = 1$. The results are presented in both log plots and log-log plots. The dashed lines correspond to fits to the last four data points, while the solid lines serve as guides to the eye.

2. Two-site operator

Next, we focus on systems with even L and choose the operator $O = Z_{L/2}Z_{L/2+1}$. Unlike the previous case, m_1 becomes nonzero in the $S_z = 0$ sector for this operator, similar to the observations in the mixed-field Ising model. However, the distinct symmetry sectors imply different finite-size scaling behaviors for $m_1(L)$. To determine $m_1(L)$, we first consider the pair of qubits at sites $L/2$ and $L/2 + 1$. Within this subspace, there are two states, $|\uparrow\uparrow\rangle$ and $|\downarrow\downarrow\rangle$, with the eigenvalue $Z_{L/2}Z_{L/2+1} = 1$, and two states, $|\uparrow\downarrow\rangle$ and $|\downarrow\uparrow\rangle$, with the eigenvalue -1 . Therefore, we expect

$$m_1(L) = 2 \frac{\binom{L-2}{\frac{L}{2}-2} - \binom{L-2}{\frac{L}{2}-1}}{\binom{L}{L/2}} = -\frac{2}{L-1} \binom{n}{k} \frac{\binom{L-1}{\frac{L}{2}-1}}{\binom{L}{\frac{L}{2}}} \sim -\frac{1}{L}. \quad (\text{A2})$$

In the second step, we invoke the identity $\binom{n}{k} - \binom{n}{k-1} = \frac{n-2k+1}{n+1} \binom{n+1}{k}$. For the final step, we employ Stirling's approximation, $n! \sim \sqrt{2\pi n} \left(\frac{n}{e}\right)^n$, to obtain the asymptotic behavior.

We then proceed to the numerical results for $F_{11} = m_2 - m_1^2$, $F_{111} = m_3 - m_1^3$, $F_{1111} = m_4 - m_1^4$, as displayed in Fig. 9. The results for additional error terms, including F_{21} , F_{31} , F_{211} , F_{22} , and $F_{211}^{(2)}$ are presented in

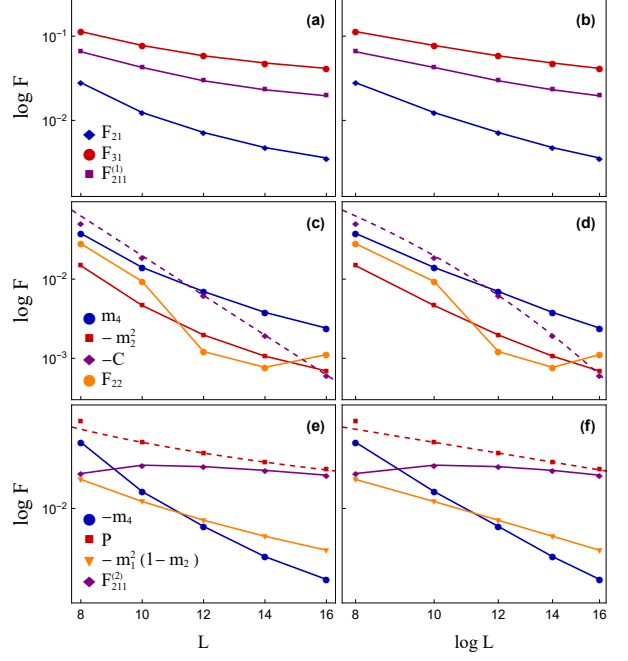


FIG. 10. Numerical results for the error terms F_{21} , F_{31} , $F_{211}^{(1)}$, F_{22} , and $F_{211}^{(2)}$ of the random-field XXZ model as a function of system size L for the two-site operator $O = Z_{L/2}Z_{L/2+1}$ with $\Delta = 1$. The results are presented in both log plots and log-log plots. The dashed lines correspond to fits to the last four data points, while the solid lines serve as guides to the eye.

TABLE IV. Fitted parameters for the two-site operator $O = Z_{L/2}Z_{L/2+1}$ of the random-field XXZ model.

Component	Model	Expression	a	b
m_1		a/L^b	1.3630	1.0890
F_{11}^L		$a \exp(-bL)$	4.1150	0.5206
F_{11}^T		a/L^b	0.3830	1.0500
F_{111}^L		$a \exp(-bL)$	—	—
F_{111}^T		a/L^b	2.2090	2.2030
F_{1111}^L		$a \exp(-bL)$	1.0440	0.5039
F_{1111}^T		a/L^b	5.6220	2.8680
C		$a \exp(-bL)$	6.6600	0.5809
P		a/L^b	0.5738	1.1810

Fig. 10. Their scaling behaviors are analogous to those observed for the single-site operators in the random-field Ising model; in particular, F_{111} exhibit a faster-than-exponential decay, similar to that for the single-site case in the mixed-field Ising model. The fitted parameters for each component are presented in TABLE. IV. In summary, we have presented numerical results for both single-site and two-site operators in the thermalized phase of the random-field XXZ model. Through the decomposition framework discussed in the main text, we

conclude that both cases validate the full ETH.

Appendix B: The level spacing ratio

In this section, we provide the level spacing ratio r for the models discussed in the main text and the preceding section. The ratio r serves as a standard diagnostic tool for identifying quantum chaos and distinguishing it from integrability.

$$r_n = \frac{\min\{s_n, s_{n+1}\}}{\max\{s_n, s_{n+1}\}}. \quad (\text{B1})$$

Here, $s_n = E_{n+1} - E_n$ denotes the spacing between adjacent energy levels, and $r = \frac{1}{D} \sum_n r_n$ is the average level spacing ratio. For chaotic systems obeying Wigner-Dyson statistics, the expected value is $r_{\text{WD}} \approx 0.5295$, whereas for integrable systems obeying Poisson statistics, $r_{\text{Poisson}} \approx 0.386$ [67, 87–90]. The level spacing ratios calculated for our parameter regimes are shown in Fig. 11. As L increases, all data points approach r_{WD} , confirming that the systems reside in the chaotic (thermalized)

regime.

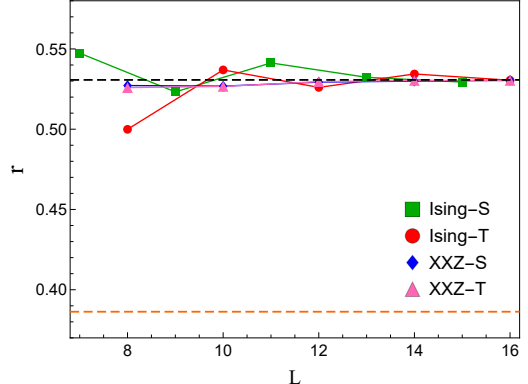


FIG. 11. Numerical results for level spacing ratios r in the mixed-field Ising and random-field XXZ models, considering both single-site and two-site operators. The black and orange dashed lines indicate the theoretical values for Wigner-Dyson and Poisson statistics, respectively. The solid lines serve as guides to the eye.

[1] M. Srednicki, Chaos and quantum thermalization, *Phys. Rev. E* **50**, 888 (1994).

[2] M. Srednicki, The approach to thermal equilibrium in quantized chaotic systems, *Journal of Physics A: Mathematical and General* **32**, 1163?175 (1999).

[3] J. M. Deutsch, Quantum statistical mechanics in a closed system, *Phys. Rev. A* **43**, 2046 (1991).

[4] J. M. Deutsch, Eigenstate thermalization hypothesis, *Rept. Prog. Phys.* **81**, 082001 (2018), arXiv:1805.01616 [quant-ph].

[5] M. Rigol, V. Dunjko, and M. Olshanii, Thermalization and its mechanism for generic isolated quantum systems, *Nature (London)* **452**, 854 (2008), arXiv:0708.1324 [cond-mat.stat-mech].

[6] R. V. Jensen and R. Shankar, Statistical behavior in deterministic quantum systems with few degrees of freedom, *Phys. Rev. Lett.* **54**, 1879 (1985).

[7] L. D’Alessio, Y. Kafri, A. Polkovnikov, and M. Rigol, From quantum chaos and eigenstate thermalization to statistical mechanics and thermodynamics, *Adv. Phys.* **65**, 239 (2016), arXiv:1509.06411 [cond-mat.stat-mech].

[8] R. Steinigeweg, J. Herbrich, and P. Prelovsek, Eigenstate thermalization within isolated spin-chain systems, *Physical Review E* **87**, 10.1103/physreve.87.012118 (2013).

[9] W. Beugeling, R. Moessner, and M. Haque, Off-diagonal matrix elements of local operators in many-body quantum systems, *Physical Review E* **91**, 10.1103/physreve.91.012144 (2015).

[10] T. Mori, T. N. Ikeda, E. Kaminishi, and M. Ueda, Thermalization and prethermalization in isolated quantum systems: a theoretical overview, *J. Phys. B* **51**, 112001 (2018), arXiv:1712.08790 [cond-mat.stat-mech].

[11] C. Nation and D. Porras, Off-diagonal observable elements from random matrix theory: distributions, fluctuations, and eigenstate thermalization, *New Journal of Physics* **20**, 103003 (2018).

[12] T. LeBlond and M. Rigol, Eigenstate thermalization for observables that break hamiltonian symmetries and its counterpart in interacting integrable systems, *Physical Review E* **102**, 10.1103/physreve.102.062113 (2020).

[13] J. D. Noh, Eigenstate thermalization hypothesis and eigenstate-to-eigenstate fluctuations, *Physical Review E* **103**, 10.1103/physreve.103.012129 (2021).

[14] M. Alishahiha and M. J. Vasli, Eigenstate Thermalization Hypothesis: A Short Review (2025) arXiv:2501.07243 [hep-th].

[15] A. M. Kaufman, M. E. Tai, A. Lukin, M. Rispoli, R. Schittko, P. M. Preiss, and M. Greiner, Quantum thermalization through entanglement in an isolated many-body system, *Science* **353**, aaf6725 (2016), arXiv:1603.04409 [quant-ph].

[16] R. Islam, R. Ma, P. M. Preiss, M. E. Tai, A. Lukin, M. Rispoli, and M. Greiner, Measuring entanglement entropy through the interference of quantum many-body twins 10.1038/nature15750 (2015), arXiv:1509.01160 [cond-mat.quant-gas].

[17] M. Rigol, V. Dunjko, V. Yurovsky, and M. Olshanii, Relaxation in a completely integrable many-body quantum system: Anabinitiostudy of the dynamics of the highly excited states of 1d lattice hard-core bosons, *Physical Review Letters* **98**, 10.1103/physrevlett.98.050405 (2007).

[18] A. Iucci and M. A. Cazalilla, Quantum quench dynamics of the luttinger model, *Physical Review A* **80**, 10.1103/physreve.80.063619 (2009).

[19] A. Polkovnikov, K. Sengupta, A. Silva, and M. Vengalattore, Colloquium: Nonequilibrium dynamics of closed in-

teracting quantum systems, *Reviews of Modern Physics* **83**, 863?83 (2011).

[20] P. Calabrese, F. H. L. Essler, and M. Fagotti, Quantum quench in the transverse-field ising chain, *Physical Review Letters* **106**, 10.1103/physrevlett.106.227203 (2011).

[21] J.-S. Caux and F. H. L. Essler, Time evolution of local observables after quenching to an integrable model, *Physical Review Letters* **110**, 10.1103/physrevlett.110.257203 (2013).

[22] V. Alba, Eigenstate thermalization hypothesis and integrability in quantum spin chains, *Physical Review B* **91**, 10.1103/physrevb.91.155123 (2015).

[23] L. Vidmar and M. Rigol, Generalized gibbs ensemble in integrable lattice models, *Journal of Statistical Mechanics: Theory and Experiment* **2016**, 064007 (2016).

[24] M. Brenes, T. LeBlond, J. Goold, and M. Rigol, Eigenstate thermalization in a locally perturbed integrable system, *Physical Review Letters* **125**, 10.1103/physrevlett.125.070605 (2020).

[25] F. Rottoli and V. Alba, Eigenstate thermalization hypothesis (eth) for off-diagonal matrix elements in integrable spin chains (2025), arXiv:2505.23602 [cond-mat.stat-mech].

[26] D. A. Abanin, E. Altman, I. Bloch, and M. Serbyn, Colloquium: Many-body localization, thermalization, and entanglement, *Rev. Mod. Phys.* **91**, 021001 (2019).

[27] F. Alet and N. Laflorencie, Many-body localization: An introduction and selected topics, *Comptes Rendus Physique* **19**, 498 (2018), arXiv:1711.03145 [cond-mat.str-el].

[28] E. Altman and R. Vosk, Universal Dynamics and Renormalization in Many-Body-Localized Systems, *Annual Review of Condensed Matter Physics* **6**, 383 (2015), arXiv:1408.2834 [cond-mat.dis-nn].

[29] R. Nandkishore and D. A. Huse, Many-Body Localization and Thermalization in Quantum Statistical Mechanics, *Annual Review of Condensed Matter Physics* **6**, 15 (2015), arXiv:1404.0686 [cond-mat.stat-mech].

[30] M. Schreiber, S. S. Hodgman, P. Bordia, H. P. Lschen, M. H. Fischer, R. Vosk, E. Altman, U. Schneider, and I. Bloch, Observation of many-body localization of interacting fermions in a quasirandom optical lattice, *Science* **349**, 842?45 (2015).

[31] A. Chandran, I. H. Kim, G. Vidal, and D. A. Abanin, Constructing local integrals of motion in the many-body localized phase, *Physical Review B* **91**, 10.1103/physrevb.91.085425 (2015).

[32] P. Ponte, Z. Papi, F. Huveneers, and D. A. Abanin, Many-body localization in periodically driven systems, *Physical Review Letters* **114**, 10.1103/physrevlett.114.140401 (2015).

[33] L. Rademaker and M. Ortuo, Explicit local integrals of motion for the many-body localized state, *Physical Review Letters* **116**, 10.1103/physrevlett.116.010404 (2016).

[34] J. Smith, A. Lee, P. Richerme, B. Neyenhuis, P. W. Hess, P. Hauke, M. Heyl, D. A. Huse, and C. Monroe, Many-body localization in a quantum simulator with programmable random disorder, *Nature Physics* **12**, 907?11 (2016).

[35] J. Z. Imbrie, On many-body localization for quantum spin chains, *Journal of Statistical Physics* **163**, 998?048 (2016).

[36] M. Serbyn, Z. Papić, and D. A. Abanin, Local conservation laws and the structure of the many-body localized states, *Phys. Rev. Lett.* **111**, 127201 (2013).

[37] D. A. Huse, R. Nandkishore, and V. Oganesyan, Phenomenology of fully many-body-localized systems, *Phys. Rev. B* **90**, 174202 (2014).

[38] R. Vosk and E. Altman, Many-body localization in one dimension as a dynamical renormalization group fixed point, *Phys. Rev. Lett.* **110**, 067204 (2013).

[39] W. Morong, F. Liu, P. Becker, K. S. Collins, L. Feng, A. Kyprianidis, G. Pagano, T. You, A. V. Gorshkov, and C. Monroe, Observation of stark many-body localization without disorder, *Nature* **599**, 393?98 (2021).

[40] Y. Patil, S. Chakram, and M. Vengalattore, Measurement-induced localization of an ultracold lattice gas, *Physical Review Letters* **115**, 10.1103/physrevlett.115.140402 (2015).

[41] A. Chan, R. M. Nandkishore, M. Pretko, and G. Smith, Unitary-projective entanglement dynamics, *Phys. Rev. B* **99**, 224307 (2019).

[42] Y. Li, X. Chen, and M. P. A. Fisher, Quantum zeno effect and the many-body entanglement transition, *Phys. Rev. B* **98**, 205136 (2018).

[43] B. Skinner, J. Ruhman, and A. Nahum, Measurement-induced phase transitions in the dynamics of entanglement, *Phys. Rev. X* **9**, 031009 (2019).

[44] S. Choi, Y. Bao, X.-L. Qi, and E. Altman, Quantum error correction in scrambling dynamics and measurement-induced phase transition, *Physical Review Letters* **125**, 10.1103/physrevlett.125.030505 (2020).

[45] Q. Tang and W. Zhu, Measurement-induced phase transition: A case study in the nonintegrable model by density-matrix renormalization group calculations, *Physical Review Research* **2**, 10.1103/physrevresearch.2.013022 (2020).

[46] S. Gherardini, G. Giachetti, S. Ruffo, and A. Trombetti, Thermalization processes induced by quantum monitoring in multi-level systems (2021), arXiv:2012.15216 [quant-ph].

[47] S. M. Walls, J. M. Schachter, H. Qian, and I. J. Ford, Stochastic quantum trajectories demonstrate the quantum zeno effect in open spin 1/2, spin 1 and spin 3/2 systems, *Journal of Physics A: Mathematical and Theoretical* **57**, 175301 (2024).

[48] J.-J. Feng and Q. Zhuang, Many-body anti-zeno thermalization and zeno determinism in monitored hamiltonian dynamics (2025), arXiv:2508.13574 [quant-ph].

[49] L. Foini and J. Kurchan, Eigenstate thermalization hypothesis and out of time order correlators, *Phys. Rev. E* **99**, 042139 (2019).

[50] S. Pappalardi, L. Foini, and J. Kurchan, Eigenstate thermalization hypothesis and free probability, *Phys. Rev. Lett.* **129**, 170603 (2022).

[51] S. Pappalardi, F. Fritzsch, and T. c. v. Prosen, Full eigenstate thermalization via free cumulants in quantum lattice systems, *Phys. Rev. Lett.* **134**, 140404 (2025).

[52] S. Jindal and P. Hosur, Generalized free cumulants for quantum chaotic systems, *Journal of High Energy Physics* **2024**, 10.1007/jhep09(2024)066 (2024).

[53] M. Fava, J. Kurchan, and S. Pappalardi, Designs via free probability, *Phys. Rev. X* **15**, 011031 (2025).

[54] H. A. Camargo, Y. Fu, V. Jahnke, K. Pal, and K.-Y. Kim, Quantum signatures of chaos from free probability (2025), arXiv:2503.20338 [hep-th].

[55] F. Fritzsch and P. W. Claeys, [Free probability in a minimal quantum circuit model](#) (2025), [arXiv:2506.11197 \[quant-ph\]](#).

[56] F. Fritzsch, T. Prosen, and S. Pappalardi, Microcanonical free cumulants in lattice systems, *Physical Review B* **111**, [10.1103/physrevb.111.054303](#) (2025).

[57] E. Vallini, L. Foini, and S. Pappalardi, [Refinements of the eigenstate thermalization hypothesis under local rotational invariance via free probability](#) (2025), [arXiv:2511.23217 \[cond-mat.stat-mech\]](#).

[58] T. Pathak, [Full Eigenstate Thermalization in Integrable Spin Systems](#), (2025), [arXiv:2510.05887 \[cond-mat.stat-mech\]](#).

[59] G. O. Alves, F. Fritzsch, and P. W. Claeys, [Probes of Full Eigenstate Thermalization in Ergodicity-Breaking Quantum Circuits](#), *Quantum* **9**, 1949 (2025), [arXiv:2504.08517 \[cond-mat.stat-mech\]](#).

[60] F. Fritzsch, G. O. Alves, M. A. Rampp, and P. W. Claeys, [Free Cumulants and Full Eigenstate Thermalization from Boundary Scrambling](#), (2025), [arXiv:2509.08060 \[quant-ph\]](#).

[61] In fact, the calculation of the two-point function is already captured by the traditional ETH ansatz (1).

[62] W. Beugeling, R. Moessner, and M. Haque, [Finite-size scaling of eigenstate thermalization](#), *Phys. Rev. E* **89**, 042112 (2014).

[63] L. D. Landau and E. M. Lifshitz, *Statistical Physics: Volume 5*, Vol. 5 (Elsevier, 2013).

[64] H. Touchette, [The large deviation approach to statistical mechanics](#), *Physics Reports* **478**, 179 (2009).

[65] M. C. Bauls, J. I. Cirac, and M. B. Hastings, [Strong and weak thermalization of infinite nonintegrable quantum systems](#), *Physical Review Letters* **106**, [10.1103/physrevlett.106.050405](#) (2011).

[66] H. Kim and D. A. Huse, [Ballistic spreading of entanglement in a diffusive nonintegrable system](#), *Physical Review Letters* **111**, [10.1103/physrevlett.111.127205](#) (2013).

[67] Y. Y. Atas, E. Bogomolny, O. Giraud, and G. Roux, [Distribution of the ratio of consecutive level spacings in random matrix ensembles](#), *Physical Review Letters* **110**, [10.1103/physrevlett.110.084101](#) (2013).

[68] Y. Y. Atas and E. Bogomolny, [Quantum ising model in transverse and longitudinal fields: chaotic wave functions](#) (2015), [arXiv:1503.04508 \[math-ph\]](#).

[69] M. Kormos, M. Collura, G. Takcs, and P. Calabrese, [Real-time confinement following a quantum quench to a non-integrable model](#), *Nature Physics* **13**, 246?49 (2016).

[70] J. D. Noh, [Operator growth in the transverse-field ising spin chain with integrability-breaking longitudinal field](#), *Physical Review E* **104**, [10.1103/physreve.104.034112](#) (2021).

[71] C. Peng and X. Cui, [Bridging quantum many-body scars and quantum integrability in ising chains with transverse and longitudinal fields](#), *Physical Review B* **106**, [10.1103/physrevb.106.214311](#) (2022).

[72] Y. Chiba, [Proof of absence of local conserved quantities in the mixed-field ising chain](#), *Physical Review B* **109**, [10.1103/physrevb.109.035123](#) (2024).

[73] R. Pirmoradian, E. Sadoogh, M. Teymour, N. Abolqasemi-Azad, M. R. Lahooti, and Z. Mohammad-Ali, [Investigation of quantum chaos in local and non-local ising models](#) (2025), [arXiv:2512.21713 \[quant-ph\]](#).

[74] A. I. Larkin and Y. N. Ovchinnikov, [Quasiclassical Method in the Theory of Superconductivity](#), *Soviet Journal of Experimental and Theoretical Physics* **28**, 1200 (1969).

[75] J. Maldacena, S. H. Shenker, and D. Stanford, [A bound on chaos](#), *JHEP* **08**, 106, [arXiv:1503.01409 \[hep-th\]](#).

[76] S. H. Shenker and D. Stanford, [Stringy effects in scrambling](#), *JHEP* **05**, 132, [arXiv:1412.6087 \[hep-th\]](#).

[77] D. A. Roberts, D. Stanford, and L. Susskind, [Localized shocks](#), *JHEP* **03**, 051, [arXiv:1409.8180 \[hep-th\]](#).

[78] S. H. Shenker and D. Stanford, [Black holes and the butterfly effect](#), *Journal of High Energy Physics* **2014**, [10.1007/jhep03\(2014\)067](#) (2014).

[79] A. Kitaev, [A simple model of quantum holography](#) (2015).

[80] K. Hashimoto, K. Murata, and R. Yoshii, [Out-of-time-order correlators in quantum mechanics](#), *Journal of High Energy Physics* **2017**, [10.1007/jhep10\(2017\)138](#) (2017).

[81] N. Lashkari, A. Dymarsky, and H. Liu, [Eigenstate Thermalization Hypothesis in Conformal Field Theory](#), *J. Stat. Mech.* **1803**, 033101 (2018), [arXiv:1610.00302 \[hep-th\]](#).

[82] M. Žnidarič, T. Prosen, and P. Prelovšek, [Many-body localization in the Heisenberg \$XXZ\$ magnet in a random field](#), *Physical Review B* **77**, 064426 (2008).

[83] A. Pal and D. A. Huse, [The many-body localization transition](#) (2010), [arXiv:1003.2613 \[cond-mat.dis-nn\]](#).

[84] D. J. Luitz, N. Laflorencie, and F. Alet, [Many-body localization edge in the random-field heisenberg chain](#), *Physical Review B* **91**, [10.1103/physrevb.91.081103](#) (2015).

[85] M. Serbyn, Z. Papi, and D. A. Abanin, [Criterion for many-body localization-delocalization phase transition](#), *Physical Review X* **5**, [10.1103/physrevx.5.041047](#) (2015).

[86] J. Untajs, J. Bona, T. Prosen, and L. Vidmar, [Quantum chaos challenges many-body localization](#), *Physical Review E* **102**, [10.1103/physreve.102.062144](#) (2020).

[87] V. Oganesyan and D. A. Huse, [Localization of interacting fermions at high temperature](#), *Physical Review B* **75**, [10.1103/physrevb.75.155111](#) (2007).

[88] A. L. Corps and A. Relaño, [Distribution of the ratio of consecutive level spacings for different symmetries and degrees of chaos](#), *Physical Review E* **101**, [10.1103/physreve.101.022222](#) (2020).

[89] G. Livan, M. Novaes, and P. Vivo, *Introduction to Random Matrices* (Springer International Publishing, 2018).

[90] F. Haake, S. Genz, and H.-J. Sommers, *Quantum Signatures of Chaos*, 4th ed. (Springer, Berlin, Heidelberg, 2018).